*remote sensing*

MDPI

*Article*

# Analytical Modeling of Electromagnetic Scattering and HRRP Characteristics from the 3D Sea Surface with a Plunging Breaker

**Chunlei Dong [1], Xiao Meng [1,*], Jinpeng Zhang [2], Yue Liu [1], Qihao Wei [1] and Lixin Guo [1]**

[1] School of Physics, Xidian University, Xi'an 710071, China; cldong@xidian.edu.cn (C.D.); yliu123@stu.xidian.edu.cn (Y.L.); qihao_wei@stu.xidian.edu.cn (Q.W.); lxguo@xidian.edu.cn (L.G.)

[2] National Key Laboratory of Electromagnetic Environment, China Research Institute of Radiowave Propagation, Qingdao 266107, China; zhangjp@crirp.ac.cn

* Correspondence: xmeng@xidian.edu.cn

**Abstract:** Electromagnetic (EM) scattering of sea surface may exhibit sea-spikespikes when there exist breaking waves. As sea-spikes are usually mistaken for targets, the investigation of EM scattering characteristics and high-range resolution profiles (HRRPs) of three-dimensional (3D) sea surfaces with a plunging breaker is meaningful for target detection and recognition. To describe the basic features of a plunging breaker, this paper developed a feasible and wind-related plunging breaker model. Here, profiles of a plunging breaker in its life cycle are modeled according to the wind speed and time factor, and the small-scale roughness is considered. Then, the sea surface and plunging breaker are combined to obtain the composite model. Additionally, a hybrid algorithm based on the Capillary Wave Modification Facet Scattering Model (CWMFSM) and ray tracing technique is developed to calculate the EM scattering of 3D sea surface with a plunging breaker. Simulation results show that the sea-spike phenomenon is more likely to occur for the upwind and large incident angles. The amplitude of the backscattering electric field from the plunging breaker is much stronger than that of the sea surface. Furthermore, the HRRPs of 3D sea surface with a plunging breaker and target are computed. Sharp peaks from the plunging breaker that exhibit obvious target-like features are observed.

**Keywords:** sea surface; plunging breaker; sea-spikes; HRRP



**Citation:** Dong, C.; Meng, X.; Zhang, J.; Liu, Y.; Wei, Q.; Guo, L. Analytical Modeling of Electromagnetic Scattering and HRRP Characteristics from the 3D Sea Surface with a Plunging Breaker. *Remote Sens.* **2023**, *15*, 2912. https://doi.org/10.3390/rs15112912

Academic Editor: Yukiharu Hisaki

Received: 11 April 2023
Revised: 29 May 2023
Accepted: 29 May 2023
Published: 2 June 2023



## 1. Introduction

In recent decades, a considerable number of studies have been conducted on the EM scattering characteristics of the sea surface [1–4]. At a low grazing angle, sea-spikes [5,6] usually occur within the sea clutter, which is primarily characterized by the scattering intensity of HH polarization exceeding that of VV polarization by as much as 10 dB or more [7]. Sea-spikes are usually mistaken for targets and may cause false target detections [8]. Meanwhile, sea-spikes have been demonstrated to correlate with breaking waves [9,10]. Hence, the investigation of EM scattering and HRRP of the 3D sea surface with a plunging breaker is meaningful for target detection and recognition.

To analyze the physical mechanism of sea-spikes, the previous works primarily focused on investigating EM scattering from the Longtank model [11], which is a series of waves generated in a wave tank representing sea waves in the phase of wave breaking. Holliday et al. [12] studied the HH and VV polarized backscattering radar cross section (RCS) for two wave groups of the Longtank model at X band with incidence angles of $\theta_i = 85^\circ, 60^\circ$ and $40^\circ$, where the sea-spike behavior is found to be more obvious at large incidence angles. West and Zhao [13,14] conducted a detailed study of the backscattering characteristics of the Longtank breaking waves based on numerical methods and analyzed the physical mechanism of sea-spikes. Meanwhile, to explore the multipath scattering from breaking waves, West et al. [15,16] extended the Longtank breaking wave by inserting a flat, horizontal section of the surface, which can provide a larger reflecting surface for multipath scattering. In their studies, the ray-optical technique was used to calculate the multipath scattering, and the simulation results indicated that multipath scattering has a great influence on the backscattering from breaking waves. Furthermore, the small-scale roughness from the two-scale model was added to the front face of Longtank waves by West [17], and the influence of small-scale roughness was discussed.

Longtank breaking waves are two-dimensional (2D) models and have a certain difference from the actual sea waves. Therefore, researchers have tried to construct the corresponding 3D breaking wave model. However, due to the unavailability of the directly measured 3D breaking wave and the complexity of the real 3D breaking wave, the simplified 3D models are adopted to explore the scattering characteristics. For example, West and Zhao et al. [18,19] extended the 2D Longtank waves uniformly in the azimuthal direction to describe the related 3D model, and the scattering characteristics were analyzed by the Multilevel Fast Multipole Algorithm (MLFMM). Li and West [20,21] investigated the microwave backscattering from 3D breaking water wave crests, where the 3D wave crests were synthesized by azimuthally aligning numerically generated 2D crests of the Longtank waves. Similarly, Zhao and West [22,23] created the 3D test crests from a series of direct 2D measurements of the time evolution of the wave tank breaker and further studied the scattering characteristics of different test profiles. According to the previous studies, we can summarize that the breaking wave is responsible for sea-spikes, which are primarily related to multipath interference and "Brewster-angle-damping". However, these previous studies were mainly based on the Longtank model, which is a series of fixed waves, and the effect of wind speed on the length and height of the breaking wave was ignored. On the other hand, multipath scattering also occurs between the sea surface and the breaking wave. Therefore, it is necessary to develop a wind-involved breaking wave model and to consider the sea surface scattering and multipath scattering between the sea surface and the breaking wave.

According to the analysis above, a feasible and wind-related 3D plunging breaker model is numerically constructed in this paper. The plunging breaker model is generated based on computer graphics [24], where the profile of a plunging breaker is modeled by a set of functions. Meanwhile, the wind speed and time factor are involved. Similar to [20,21], the primary 3D plunging breaker is established by aligning a series of time factors in the numerically generated 2D plunging breakers at first. However, the primary 3D plunging breaker is limited to a smooth surface and cannot reveal the real sea wave. Therefore, the 3D plunging breaker model is additionally formed on the basis of a two-scale model [17], where the small-scale roughness is considered. Finally, the spline interpolation is applied to connect the 3D sea surface and plunging breaker to obtain the 3D composite model. This model can provide a brief description of the time evolution of the 3D sea surface with a plunging breaker. In order to compute the EM scattering, a hybrid algorithm, which combines the CWMFSM [25] with the ray tracing technique, is developed. As we aim at the influence of plunging breaker profiles on EM scattering characteristics during its generation process, four typical profiles at different stages of breaking are calculated in this paper. At the same time, the sea-spike phenomenon for different profiles and wind speeds is discussed.

Moreover, it is known that HRRP is considered one of the important features of radar in the remote sensing field. Sea-spikes may exhibit features similar to those of targets and are usually mistaken for targets. Therefore, exploring the HRRP characteristics of the 3D sea surface with a plunging breaker is significant for target detection and recognition. However, to our knowledge, the previous studies were primarily limited to the EM scattering characteristics of Longtank model. At the same time, little research has been carried out on the HRRP characteristics. For this reason, our work is further extended to the investigation of HRRP characteristics of the 3D sea surface with a plunging breaker. The HRRPs for sea surfaces with and without a plunging breaker are compared. Meanwhile, the influence of a plunging breaker on the HRRP of maritime targets is further discussed. According to the simulation results, some noticeable target-like features are observed when there exists a plunging breaker, which will greatly impact on target detection and recognition.

The remainder of this paper is arranged as follows. In Section 2, the EM scattering modeling process of the 3D sea surface with a plunging breaker is described. Additionally, the EM scattering and HRRP characteristics from 3D sea surface with a plunging breaker and target are discussed in Section 3. Section 4 ends with a summary of this paper.

## 2. EM Scattering Modeling of the 3D Sea Surface with a Plunging Breaker

### *2.1. Geometric Modeling of the 3D Sea Surface with a Plunging Breaker*

Geometric modeling of the 3D sea surface with a plunging breaker is of great importance for EM scattering calculation. In view of the complexity of the real breaking waves, a feasible and wind-related 3D plunging breaker model is numerically generated in this paper. Compared with the Longtank model, the advantage of taking wind speed into consideration is that it allows us to conveniently combine the plunging breaker with the sea surface. In the following, the construction of a 3D sea surface with a plunging breaker will be introduced in detail.

#### 2.1.1. Construction of the Primary 3D Plunging Breaker

According to [26], the relationship between the height of a sea wave and the wind speed can be approximately expressed as

$$H = 17.03 \cdot \exp(-\frac{\alpha^2}{18.3269}) + 2.361 \cdot \exp(-\frac{\beta^2}{8.8646}) \tag{1}$$

where $\alpha = u^{2/3} - 12.6549$, $\beta = u^{2/3} - 6.4463$, $H$ is the height of a sea wave, and $u$ is the wind speed 10 m above sea surface.

Assume that $S$ represents the wave steepness, which is defined as the ratio of the wave height and wavelength,

$$S = H/L \tag{2}$$

where $L$ is the length of the sea wave.

Substituting Equation (1) into Equation (2), the length of a sea wave can be obtained,

$$L = 17.03 \cdot \exp(-\frac{\alpha^2}{18.3269})/S + 2.361 \cdot \exp(-\frac{\beta^2}{8.8646})/S \tag{3}$$

Next, the plunging breaker model, which is related to the wind speed, is constructed according to Equations (1)–(3) and the computer graphics [24], where the time evolution of the waves is modeled using a set of functions. The basic "life cycle" of a plunging breaker consists of the round stage, breaking stage, and collapsing stage.

During the generation process of a plunging breaker, the function parameterization is blended over time. As the front and back parts of a plunging breaker have different profiles, the space parameter $s(0 \leq s \leq 1)$ is split for the front and back part, where the wave lip is defined by $s = 0.5$. The parameters $s_1$ and $s_2$ are also computed for the two cases and can be expressed as:

$$\begin{cases} s_1 = \frac{(2s)^{k_1}}{2} \\ s_2 = (2s)^{k_1} \end{cases} (0 \leq s \leq 0.5), \begin{cases} s_1 = \frac{1+(2s-1)^{k_1}}{2} \\ s_2 = 1-(2s-1)^{k_1} \end{cases} (0.5 \leq s \leq 1) \tag{4}$$

Then, the coordinates $(x, z)$ are calculated by the following functions,

$$\begin{cases} x = L \cdot ((0.5 - s_1)\cos(\varphi) - r\sin(\varphi) + 0.5) \\ z = H \cdot z'/z_{\max} = H \cdot [(0.5 - s_1)\sin(\varphi) + r\cos(\varphi)]k_7/z_{\max} \end{cases} \tag{5}$$

where $r = k_2(1 + \cos((s_2 - 1)\pi))/2 + k_3 s_2^{k_4}$, $\varphi = \pi k_5 s_2^{k_6}/2$, $z_{\max} = max\{z'\}$.

$k_1 \sim k_7$ vary with the parameter $t$ during the generation process and are used to control the profiles of the plunging breaker at different time sampling points. Similarly, the calculation of $k_1 \sim k_7$ is split for the front and back part of the plunging breaker, which can be obtained in [24].

The profiles of a plunging breaker at the breaking stage were mainly discussed in this paper. By using Equations (1)–(5), profiles of a plunging breaker at the breaking stage for sixteen different time sampling points are generated, which is given in Figure 1. Here, the wind speeds are $u$ = 7 m/s and $u$ = 10 m/s. The direction of the wind is along the -$x$ axis. In particular, the wave steepness is chosen as $S = 1/7$ according to Stokes' theory for a sea wave at the onset of breaking. It is seen that the height and length of the plunging breaker increased during the generation process and with the wind speed. Therefore, the evolution of a 2D plunging breaker at the breaking stage is obtained.

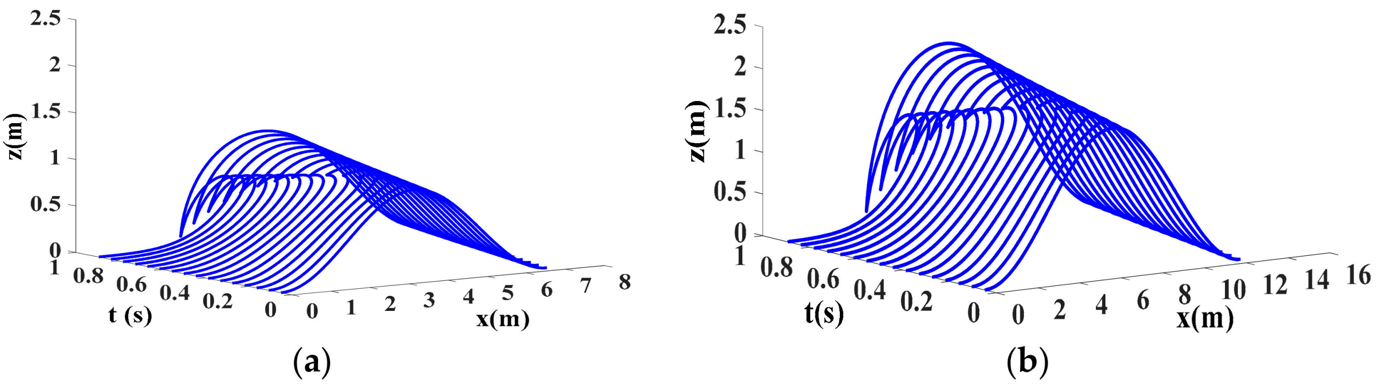


**Figure 1.** Profiles of a plunging breaker at the breaking stage for (**a**) $u$ = 7 m/s, (**b**) $u$ = 10 m/s.

In order to build the primary 3D plunging breaker, the 2D plunging breakers in neighboring time factors are aligned in the azimuthal direction, which is similar to that in [20,21]. It should be pointed out that the primary 3D plunging breaker is limited to a smooth surface, and more complex features are not considered. Therefore, further improvement is conducted in the following section.

2.1.2. Construction of the 3D Sea Surface with a Plunging Breaker

To achieve a more reasonable 3D plunging breaker model, the small-scale roughness is further considered. This idea comes from the concept of a two-scale model, which was also used in [17]. The rough 3D plunging breaker is envisaged as a two-scale profile. The macroscopic profile is represented by the primary 3D plunging breaker, and the small-scale roughness that represents the microscopic profile is added to the primary 3D plunging breaker. In this paper, the high-frequency component of Elfouhaily (ELH) [27] spectrum is adopted to generate the small-scale roughness via the Monte Carlo method.

Figure 2 illustrates the flowchart of geometric modeling of the 3D sea surface with a plunging breaker. Given the wind speed and direction, the rough 3D plunging breaker with small-scale roughness is generated, as mentioned above. The 3D sea surface is modeled via the Monte Carlo method, where the ELH spectrum is utilized. Usually, the wave steepness $S = 1/7$ is the main threshold for wave breaking. Therefore, the region of the sea surface with a wave steepness that is close to $S = 1/7$ is considered the plunging breaker region and is replaced by a 3D plunging breaker. Finally, the spline interpolation is used to treat the boundary between the sea surface and the plunging breaker, ensuring the continuity of the 3D composite model.

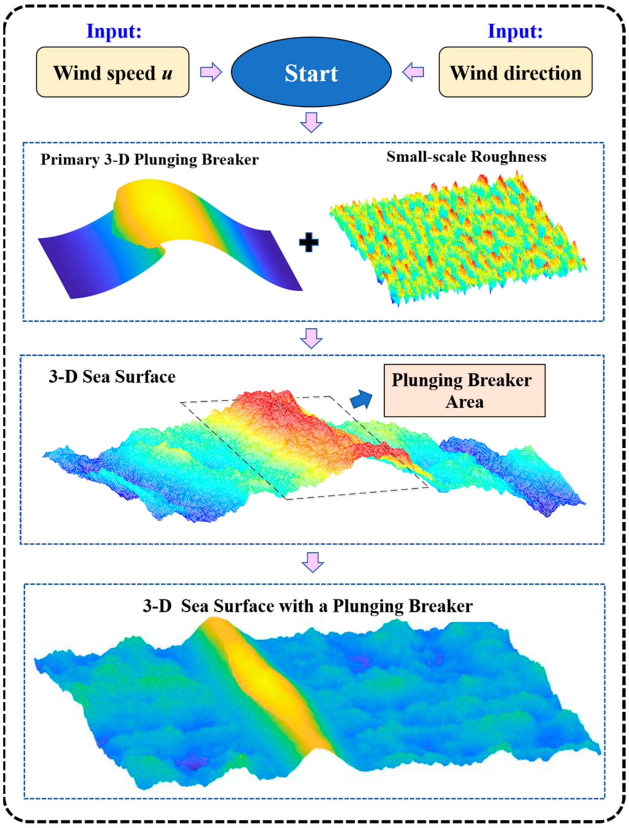


**Figure 2.** Flowchart of geometric modeling of the 3D sea surface with a plunging breaker.

Figures 3 and 4 present four profiles of the 3D sea surface with a plunging breaker at different time sampling points. The wind speeds are $u$ = 7 m/s and 10 m/s, respectively. The four test profiles represent four typical structures occurring in different stages of breaking, which are 60 m and 30 m in length and width. The time sampling interval $\Delta t = T/(N_t - 1)$, where $T$ is the life cycle of a plunging breaker and $N_t$ is the number of time sampling points.

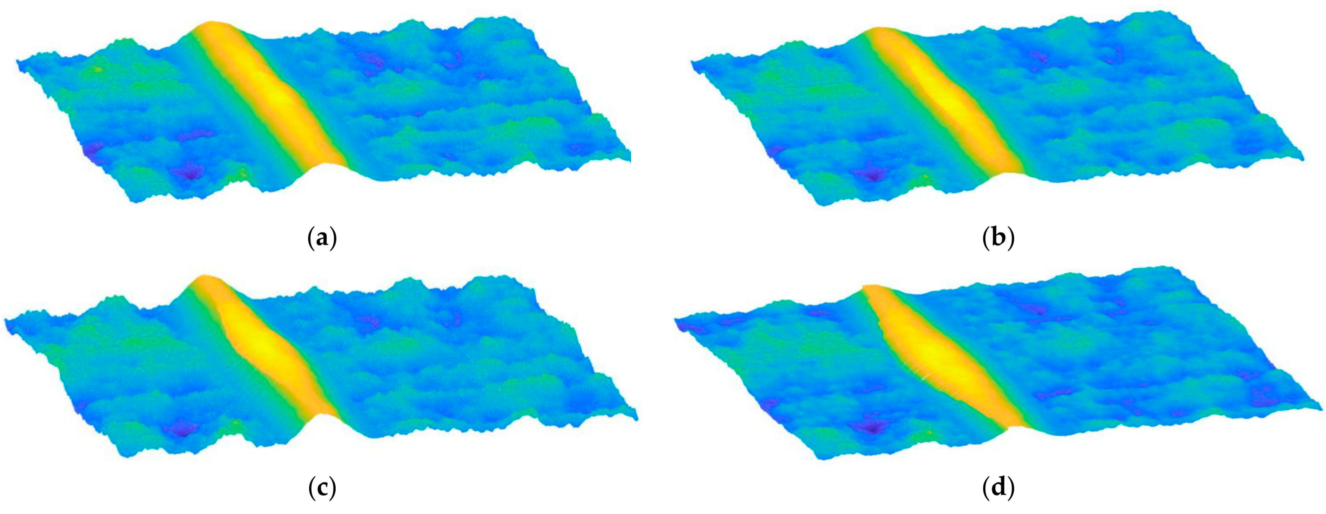

**Figure 3.** The 3D sea surface with a plunging breaker ($u$ = 7 m/s): (**a**) $t = \Delta t$, (**b**) $t = 6\Delta t$, (**c**) $t = 10\Delta t$, (**d**) $t = 14\Delta t$.

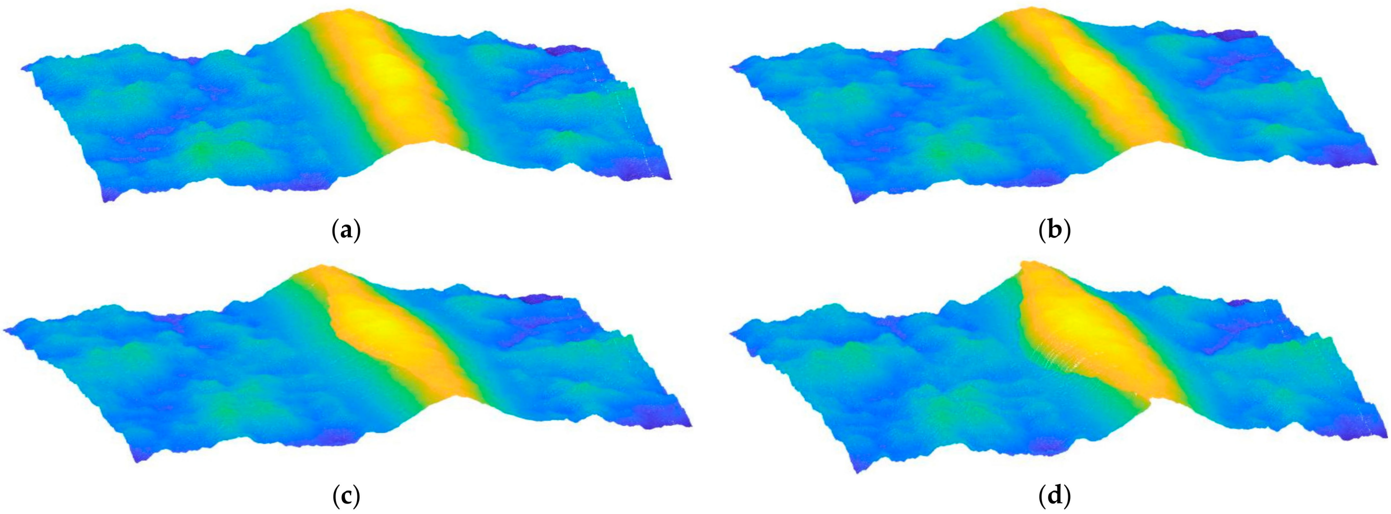


**Figure 4.** The 3D sea surface with a plunging breaker ($u$ = 10 m/s): (**a**) $t = \Delta t$, (**b**) $t = 6\Delta t$, (**c**) $t = 10\Delta t$, (**d**) $t = 14\Delta t$.

As shown in Figures 3 and 4, the steepening profile of the plunging breaker was not observed at $t = \Delta t$. With the time stepping, more complex wave shapes were generated, and the curly crests in the profiles occurred. As presented, the models in this paper can reflect the time evolution of the 3D sea surface with a plunging breaker at different stages of breaking.

### 2.2. EM Scattering Modeling of the 3D Sea Surface with a Plunging Breaker

In this paper, a hybrid algorithm based on CWMFSM, and ray tracing technique is developed to compute the EM scattering of the 3D sea surface with a plunging breaker.

Let us consider an incident EM wave that illuminates the system, as shown in Figure 5. The model is divided into three regions: Region_1, Region_2, and Region_3. Region_1 and Region_3 represent the sea surface area, and Region_2 represents the plunging breaker area. EM scattering from the 3D sea surface with a plunging breaker consists of three parts: (I) EM scattering from the sea surface (Region_1 and Region_3); (II) EM scattering from the plunging breaker (Region_2); (III) Coupling scattering between the sea surface and plunging breaker, which can be expressed as

$$\vec{E}_s = \vec{E}_{sea} + \vec{E}_{breaker} + \vec{E}_{coup} \tag{6}$$

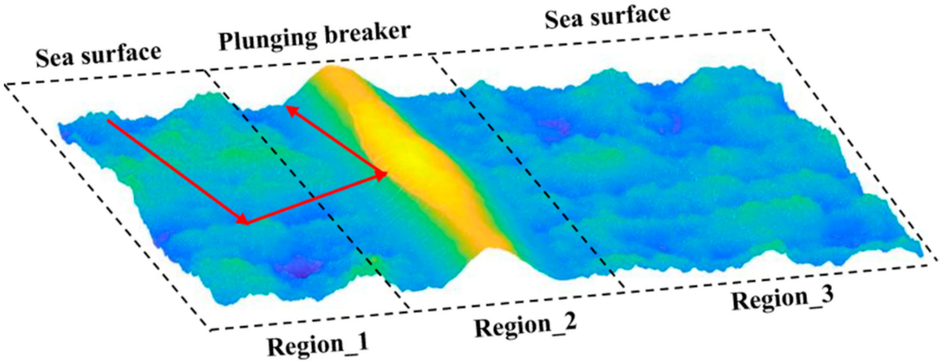


**Figure 5.** Scattering from the 3D sea surface with a plunging breaker (The red arrows represent the coupling path).

In Equation (6), the EM scattering from sea surface $\vec{E}_{sea}$ is computed by the CWMFSM, and the EM scattering from plunging breaker $\vec{E}_{breaker}$ and the coupling scattering between sea surface and plunging breaker $\vec{E}_{coup}$ are calculated by the ray tracing technique.

#### 2.2.1. CWMFSM

CWMFSM [25] is established based on the two-scale model of sea surface, where the large-scale roughness of sea surface is constructed as a series of tilted triangle facets based on the Monte Carlo Method, and the small-scale roughness of each tilted facet is assumed to be a sinusoidal wave, which can cause the Bragg scattering. Therefore, the profile of small-scale capillary wave $\zeta(\vec{r})$ is:

$$\zeta(\vec{\rho}_c, t) = B(\vec{k}_c)\cos(\vec{k}_c \cdot \vec{\rho}_c - \omega_c t) \tag{7}$$

where $\vec{k}_c$ is the wave number vector of the small-scale capillary wave. $\omega_c$ is the spatial frequency of $\vec{k}_c$. $\vec{\rho}_c = (x_c, y_c)$ denotes the position of each point on the tilted facet.

In Equation (7), $B(\vec{k}_c)$ represents the amplitude of the small-scale capillary wave, which can be expressed as:

$$B(\vec{k}_c) = 2\pi\sqrt{S_E^{capi}(\vec{k}_c)/\Delta S} \tag{8}$$

where $\Delta S = \Delta x \Delta y$ is the area of the tilted facet, and $S_E^{capi}$ is the spectrum of the small-scale capillary wave.

The scattered field from each tilted facet is calculated by integrating on the small-scale roughness at specified profile:

$$\vec{E}_{pq}^{scatt}(\hat{k}_i, \hat{k}_s) = \frac{e^{ikR_0}}{iR_0}\frac{k^2(1-\varepsilon_r)}{4\pi}F_{pq}\iint \zeta(\vec{r})\, e^{-i\vec{q}\times\vec{r}}\, d\vec{r} \tag{9}$$

where $k$ is the wavenumber of incident wave, and $\varepsilon_r$ is the relative permittivity of the seawater. $R_0$ is the distance between the radar position and center of facet. $\hat{k}_i$ and $\hat{k}_s$ are the direction of incident and scattered wave vector, respectively. $\vec{q} = k(\hat{k}_s - \hat{k}_i)$, and $F_{pq}$ represents the polarization factors. Referring to [25], more details can be obtained.

Accordingly, the scattered field from the sea surface is the summation of the scattered field of each tilted facet:

$$\vec{E}_{sea}(\hat{k}_i, \hat{k}_s) = \sum_{i=1}^{M} \vec{E}_{pq,i}^{scatt}(\hat{k}_i, \hat{k}_s) \tag{10}$$

where $M$ is the number of sea facets.

To confirm the validity of CWMFSM for EM scattering of the sea surface, the simulated results are compared with the experimental data in [28], as shown in Figure 6. The sea surface is 512 m × 512 m, and the wind speeds are $u$ = 5 m/s and 10 m/s. The relative permittivity of seawater is $\varepsilon_r = (44.1106, 39.6203)$, which is computed by the Debye model [29]. The frequency of an incident wave is $f$ = 14 GHz. Additionally, the simulated backscattering coefficient by CWMFSM represents the backscatter of the ensemble average of 30 sea surface samples. It is observed that the results show a good agreement between the CWMFSM and experimental data for both HH and VV polarization. Thus, the validity of CWMFSM for sea surface scattering calculation is proved.

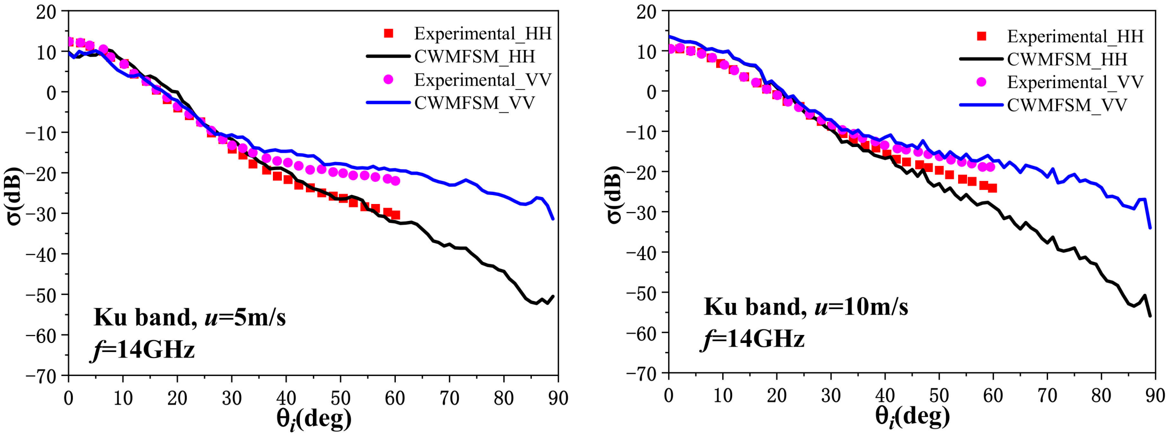


(**a**) (**b**)

**Figure 6.** Comparison of backscattering coefficient from 3D sea surface between the CWMFSM and experimental data: (**a**) $u$ = 5 m/s, (**b**) $u$ = 10 m/s.

Furthermore, the comparison results between the CWMFSM and Two-scale Model (TSM) for the X band are depicted in Figure 7, where the frequency of incident wave is $f$ = 10 GHz and $\varepsilon_r = (54.6489, 38.5679)$. Figure 7 shows that the backscattering coefficients of 3D sea surface simulated by CWMFSM are consistent with those of TSM. Therefore, it indicates that CWMFSM is efficient for EM scattering prediction of the 3D sea surface.

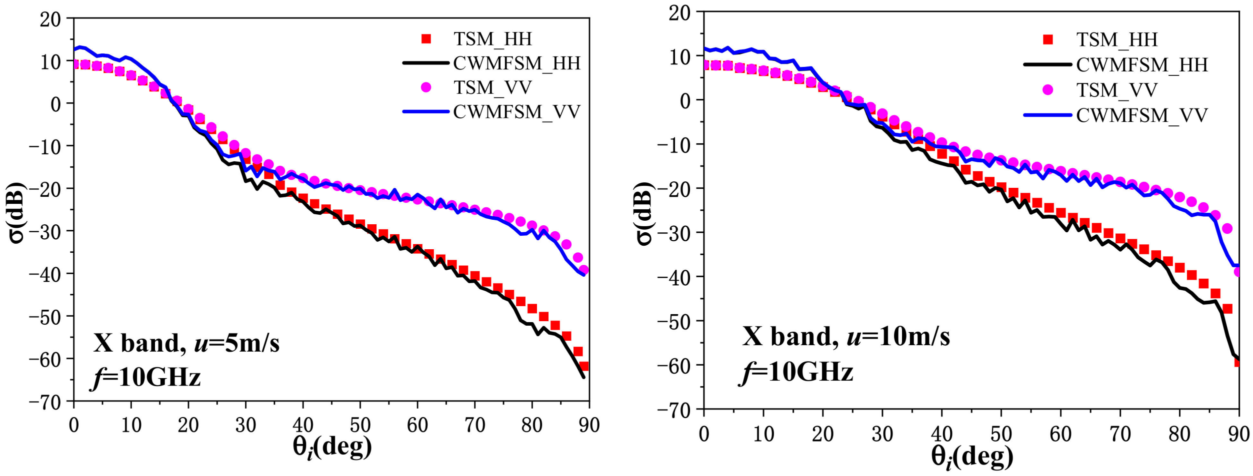


(**a**) (**b**)

**Figure 7.** Comparison of backscattering coefficient from 3D sea surface between CWMFSM and TSM: (**a**) $u$ = 5 m/s, (**b**) $u$ = 10 m/s.

### 2.2.2. Ray Tracing Technique

According to past research, multipath scattering has been considered a main contributor to sea-spikes. In practice, although the CWMFSM is useful for EM scattering from the 3D sea surface, it cannot deal with the multipath scattering caused by the plunging breaker. Thus, the ray tracing technique, which is famous for its efficiency in calculating the multipath scattering of the 3D complex object [30], is selected to calculate the EM scattering from the plunging breaker and the multipath scattering (coupling scattering) between the sea surface and plunging breaker.

In this paper, the multipath scattering occurs not only between the different facets of the plunging breaker, but also between the sea surface and the plunging breaker. The advantage of using the ray tracing technique becomes clear since it provides a feasible way to calculate these two kinds of multipath scattering. For the ray tracing technique, as presented in Figure 8, the initial rays are launched from the incident direction and pass through the center of each facet. Then, each ray is traced according to the principle of Geometric Optics (GO) until it does not intersect with any facet.

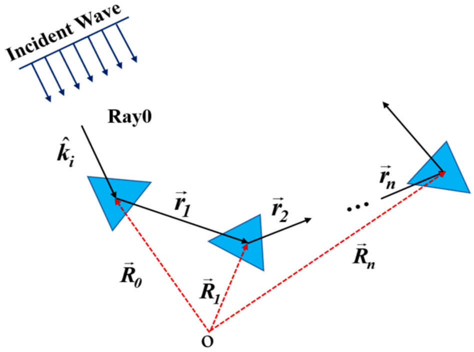


**Figure 8.** Ray tracing technique.

Assume that a ray intersects with several facets at points $\vec{R}_0, \vec{R}_1 \cdots \vec{R}_n$ in the ray tracing process. The electric field between two neighbor intersections can be computed based on GO:

$$\vec{E}\left(\vec{R}_{i+1}\right) = (\overline{\Gamma})_{\mathrm{i}} \vec{E}\left(\vec{R}_i\right) e^{-jkR} \tag{11}$$

where $\vec{E}(\vec{R}_i)$ represents the incident field at the $i$th reflection point $\vec{R}_i$. $R = \left|\vec{R}_{i+1} - \vec{R}_i\right|$ is the distance between two neighboring reflection points. $(\overline{\Gamma})_i$ is the planar reflection coefficient matrix at the reflection point.

The scattering field from the lighted facet is computed based on the Physical Optics (PO) [31]. The scattering field from all the lighted facets is summed to obtain the scattering field from the plunging breaker $\vec{E}_{breaker}$ and the multipath scattering between the sea surface and the plunging breaker $\vec{E}_{coup}$, which can be expressed as:

$$\vec{E}_{breaker} + \vec{E}_{coup} = \sum_{i=1}^{N} \vec{E}_i^{\,s} \tag{12}$$

where $N$ is the number of lighted facets.

Moreover, the well-known Oct-tree structure [32] is utilized to accelerate the ray tracing process. Meanwhile, the neighbor search technique, which has been published in our previous work [33], is combined with the Oct-tree structure to further decrease the intersection tests and improve the computational efficiency of ray tracing.

The performance of the ray tracing technique is further demonstrated by comparing it with the simulated results of MLFMM-FEKO. As the limitation of computational time and memory of MLFMM, the backscattering RCS from a local sea surface with a plunging breaker is calculated, whose size is scaled to 0.54 m × 0.6 m. The frequency of an incident wave is $f$ = 10 GHz and $\varepsilon_r = (54.6489, 38.5679)$. The profile of the 3D local sea surface with a plunging breaker is shown in Figure 9, and the simulation results are compared in Figure 10. When the incident azimuth angle $\varphi_i = 0^\circ$, the incident angle $\theta_i$ varying from $-90^\circ$ to $0^\circ$ means upwind incidence, whereas incident angle $0^\circ \sim 90^\circ$ means downwind incidence. As shown in Figure 10, backscattering RCS by ray tracing model shows a good agreement with those of MLFMM-FEKO. The simulation time for the ray tracing and MLFMM-FEKO is 27.8 s and 154 min, respectively. Therefore, the validity of the ray tracing technique is proved.

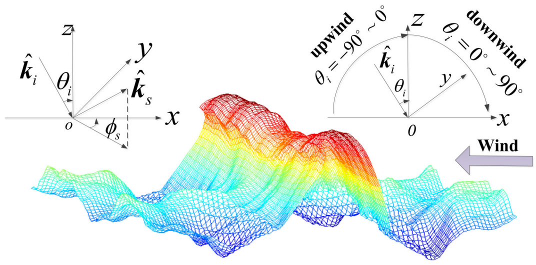


**Figure 9.** Profile of the 3D local sea surface with a plunging breaker.

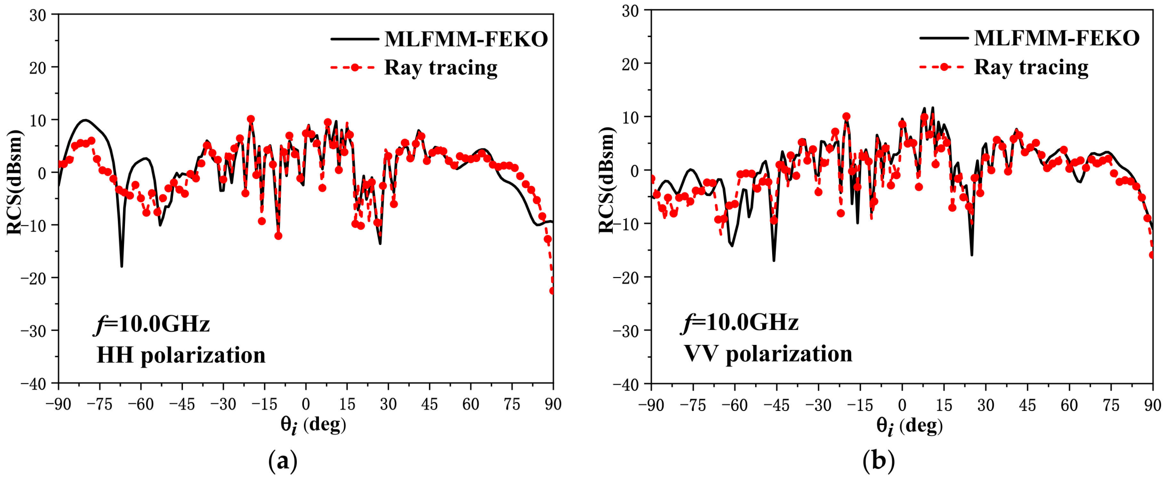


**Figure 10.** Comparison of backscattering RCS from the 3D local sea surface with a plunging breaker between the MLFMM-FEKO and Ray tracing technique: (**a**) $f$ = 10 GHz, HH polarization, (**b**) $f$ = 10 GHz, VV polarization.

## 3. Results

This section evaluates the backscattering and HRRP characteristics of the 3D sea surface with and without a plunging breaker at the X band ($f$ = 10.0 GHz). The permittivity of seawater is $\varepsilon_r = (54.6489, 38.5679)$. Typically, four profiles at $t = \Delta t, 6\Delta t, 10\Delta t, 14\Delta t$ are considered. The size of the sea surface is set as 150 m $\times$ 30 m. Figure 11 illustrates the scattering of the 3D sea surface with a plunging breaker.

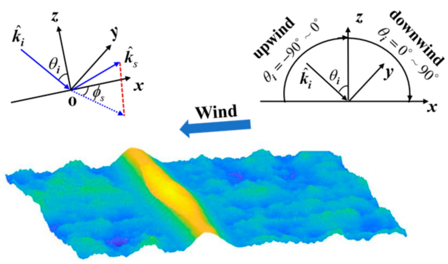


**Figure 11.** The Scattering of 3D sea surface with a plunging breaker.

### 3.1. Backscattering Radar Cross Section

Figures 12–14 depict the backscattering RCS of the 3D sea surface with and without a plunging breaker. The wind speeds are $u$ = 7 m/s, 10 m/s, and 15 m/s, respectively. The incident azimuth angle is $\varphi_i = 0°$. Simulation results are averaged over 30 samples.

As shown in Figure 12a, with the increase in incident angle, the backscattering RCS of HH polarization becomes smaller than that of VV polarization for the sea surface without a plunging breaker. Sea-spike behavior (backscattering RCS of HH polarization exceeding that of VV polarization) is not observed. In contrast, when there exists a plunging breaker on the sea surface (Figure 12b–e), the backscattering RCS changed, and sea-spikes occurred during the time evolution of the plunging breaker. First, considering profile 1 at $t = \Delta t$, the plunging breaker is at the very beginning of generation. The size of plunging breaker is small, and the wave is not steepening. Therefore, the sea surface scattering performs the dominant role, and the sea-spike behavior does not take place at $t = \Delta t$, as presented in Figure 12b. With the time stepping, the sea wave gradually steepened, and the increasing multipath scattering also has a great impact on the simulation results. Compared with Figure 12b, the backscattering RCS is significantly enhanced for the upwind incidence at $t = 6\Delta t, 10\Delta t, 14\Delta t$ in Figure 12c–e. Correspondingly, the phenomenon of backscattering RCS of HH polarization exceeding that of VV polarization is apparent, which is marked in the dotted regions. Here, sea-spike phenomenon is produced at approximately $\theta_i = [-90°, -66°]$, $[-90°, -60°]$, and $[-90°, -55°]$ in Figure 12c–e. Note that the sea spike phenomenon is more likely to occur for the upwind and large incident angles, where the front face of the plunging breaker is irradiated, and a strong multipath scattering effect occurs. Sea spike phenomenon is primarily due to multipath interference and "Brewster-angle-damping". When the incident angle is close to the Brewster angle of the seawater dielectric constant, the VV multipath is greatly attenuated and causes the sea-spike phenomenon. Moreover, the number of incident angles where the sea-spike phenomenon occurred appears to increase with the time stepping during the process of plunging breaker generation. This result also benefits from the increase in the multipath scattering effect.

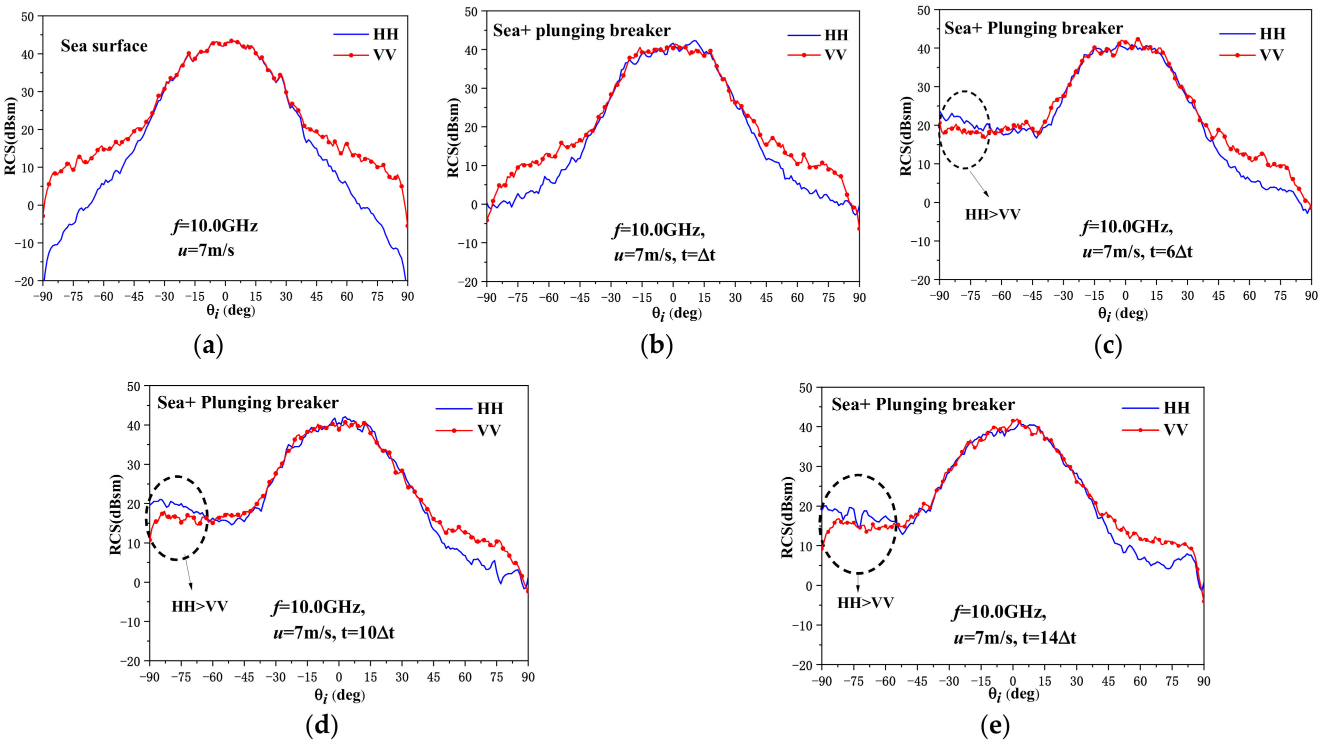


**Figure 12.** Backscattering RCS for the 3D sea surface with and without a plunging breaker ($u$ = 7 m/s): (**a**) sea surface, (**b**) sea + plunging breaker: $t = \Delta t$, (**c**) sea + plunging breaker: $t = 6\Delta t$, (**d**) sea + plunging breaker: $t = 10\Delta t$, (**e**) sea + plunging breaker: $t = 14\Delta t$.

Figures 13 and 14 present the backscattering RCS for $u$ = 10 m/s and 15 m/s. Similar to Figure 12, the backscattering RCS of VV polarization is larger than that of HH polarization for the sea surface without a plunging breaker, as shown in Figures 13a and 14a. Meanwhile, the multipath scattering between the sea surface and plunging breaker for profile 1 is weak compared with the total scattering fields, and the sea-spike phenomenon is hardly observed at $t = \Delta t$ in Figures 13b and 14b. While the sea wave is breaking over time, a more complex profile of the plunging breaker, including an overturning crest, arises. As seen in Figures 13c–e and 14c–e, the backscattering RCS of HH polarization exceeds that of VV polarization at $t = 6\Delta t, 10\Delta t, 14\Delta t$ for an upwind incidence.

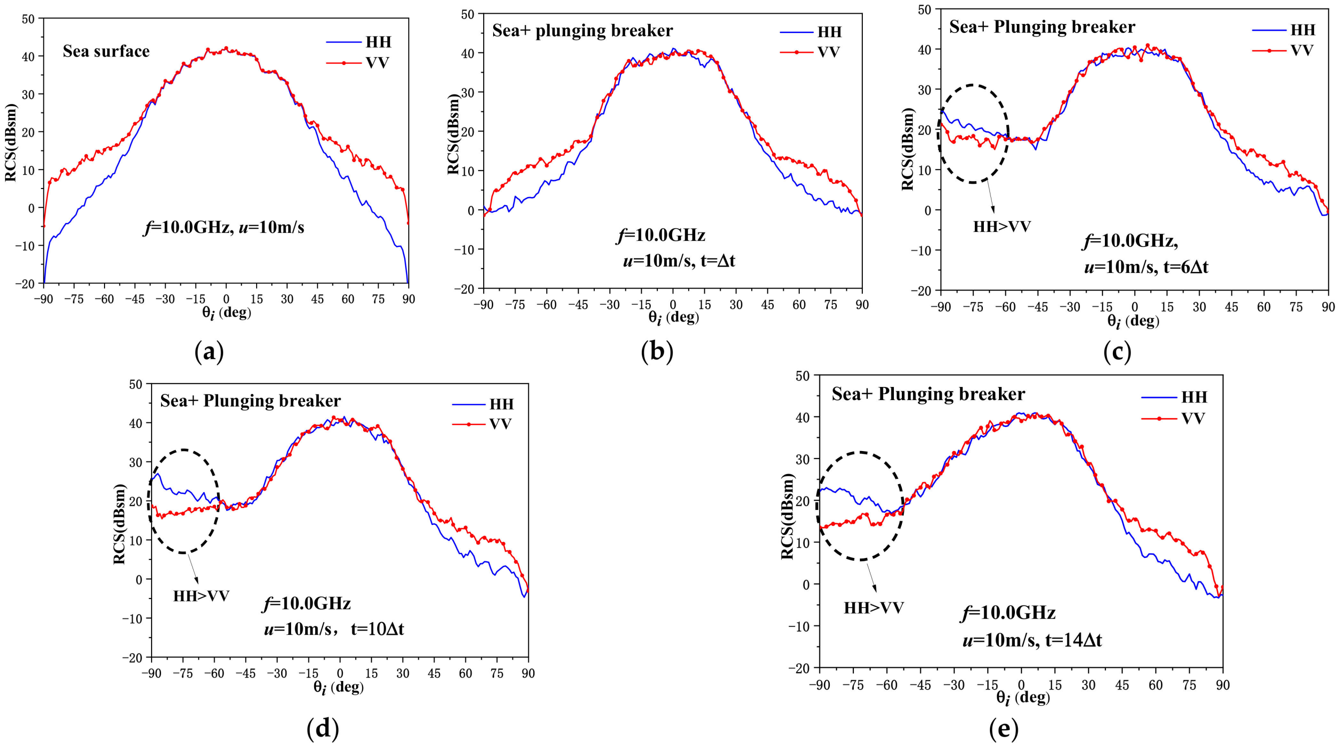


**Figure 13.** Backscattering RCS for the 3D sea surface with and without a plunging breaker ($u$ = 10 m/s): (**a**) sea surface, (**b**) sea + plunging breaker: $t = \Delta t$, (**c**) sea + plunging breaker: $t = 6\Delta t$, (**d**) sea + plunging breaker: $t = 10\Delta t$, (**e**) sea + plunging breaker: $t = 14\Delta t$.

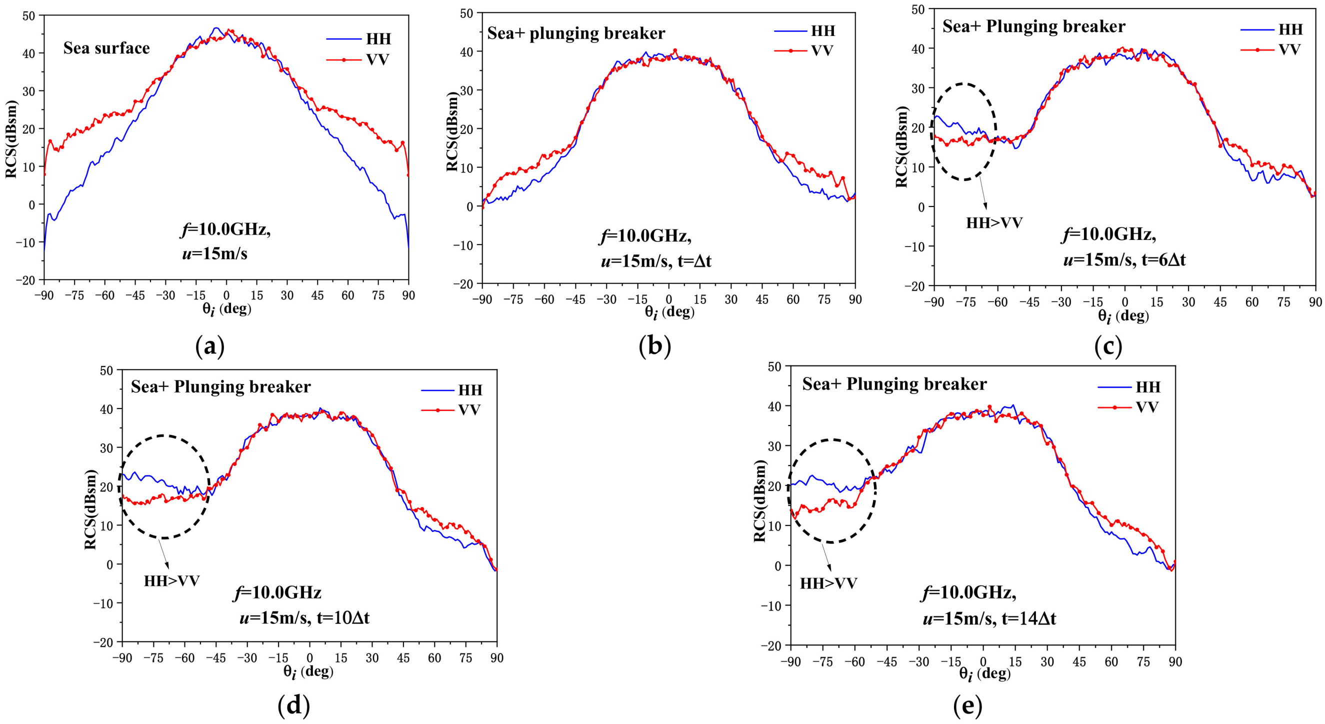


**Figure 14.** Backscattering RCS for the 3D sea surface with and without a plunging breaker ($u$ = 15 m/s): (**a**) sea surface, (**b**) sea + plunging breaker: $t = \Delta t$, (**c**) sea + plunging breaker: $t = 6\Delta t$, (**d**) sea + plunging breaker: $t = 10\Delta t$, (**e**) sea + plunging breaker: $t = 14\Delta t$.

In order to provide the quantitative evidence as to the dependency of sea-spike observations with wind speed, a histogram that shows the number of incidence angles where HH > VV for different wind speeds is presented in Figure 15. Since sea spike phenomenon of HH > VV is hardly observed for $t = \Delta t$, the time sampling points are set as $t = 6\Delta t, 10\Delta t, 14\Delta t$. According to the statistical results in Figure 15, it is found that the number of incidence angles where HH > VV increased with the wind speed. Therefore, sea-spike phenomenon becomes more obvious with the increase in wind speed. This is caused by the fact that the roughness of sea surface and the size of plunging breaker increased with the wind speed, resulting in the increase in multipath scattering.

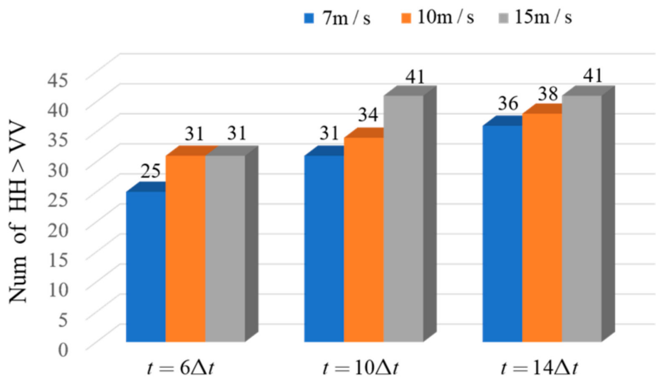


**Figure 15.** Number of incidence angles where HH > VV for different wind speeds.

The simulation results of Figures 12–15 demonstrate that the plunging breaker is responsible for sea-spike phenomenon. The profile of a plunging breaker has a significant effect on the EM scattering results. Meanwhile, the sea-spike phenomenon appears to be more obvious during the generation process of the plunging breaker. As the front face (steep part) of the plunging breaker is lighted for the upwind incidence, the backscattering RCS varies more dramatically than that of the downwind incidence. In addition, the sea-spike phenomenon is more likely to occur for large incident angles, upwind incidence, and a large wind speed.

### *3.2. Spatial Distribution of the Backscattering Electric Field*

The spatial distributions of the normalized backscattering electric field from the 3D sea surface with and without a plunging breaker are shown in Figures 16 and 17, respectively. The wind speeds are $u$ = 7 m/s and $u$ = 10 m/s. The incident angle is $\theta_i = -75°$ and HH polarization is considered. The other parameters are identical to those of Figures 12 and 13.

Figures 16 and 17 indicate that the existence of a plunging breaker can cause significant changes in the spatial distribution of the backscattering electric field for a large incident angle. The amplitude of the backscattering electric field from the plunging breaker region is much higher than that the of sea surface. In particular, the crest region of the plunging breaker, which includes a complex and steep structure, is more apparent and much brighter than that of the other region of the plunging breaker. This result means that the strong echo primarily comes from the plunging breaker region and exhibits sharp and short bursts in the sea background clutter, which contributes to the sea-spike phenomenon. Additionally, the variation in the profile of a plunging breaker has a great effect on the calculated spatial distribution of the backscattering electric field. With time stepping, a stronger echo is produced by the crest of the plunging breaker at $t = 6\Delta t, 10\Delta t, 14\Delta t$. At the same time, the difference in backscattering electric field intensity between the sea region and plunging breaker region becomes larger than that of $t = \Delta t$. Therefore, the spatial distribution images the of sea region in Figures 16c–e and 17c–e is darker than that of Figures 16b and 17b.

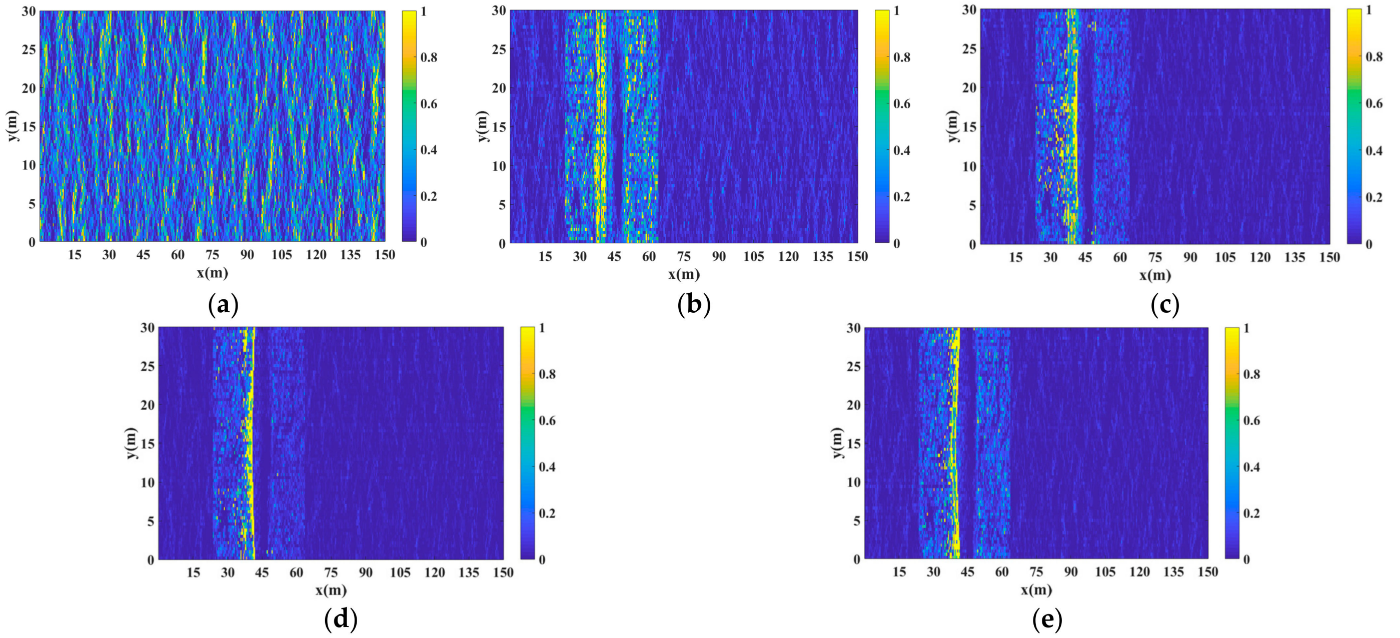


**Figure 16.** Spatial distribution images of the normalized backscattering electric field ($u$ = 7 m/s): (**a**) sea surface, (**b**) sea + plunging breaker: $t = \Delta t$, (**c**) sea + plunging breaker: $t = 6\Delta t$, (**d**) sea + plunging breaker: $t = 10\Delta t$, (**e**) sea + plunging breaker: $t = 14\Delta t$.

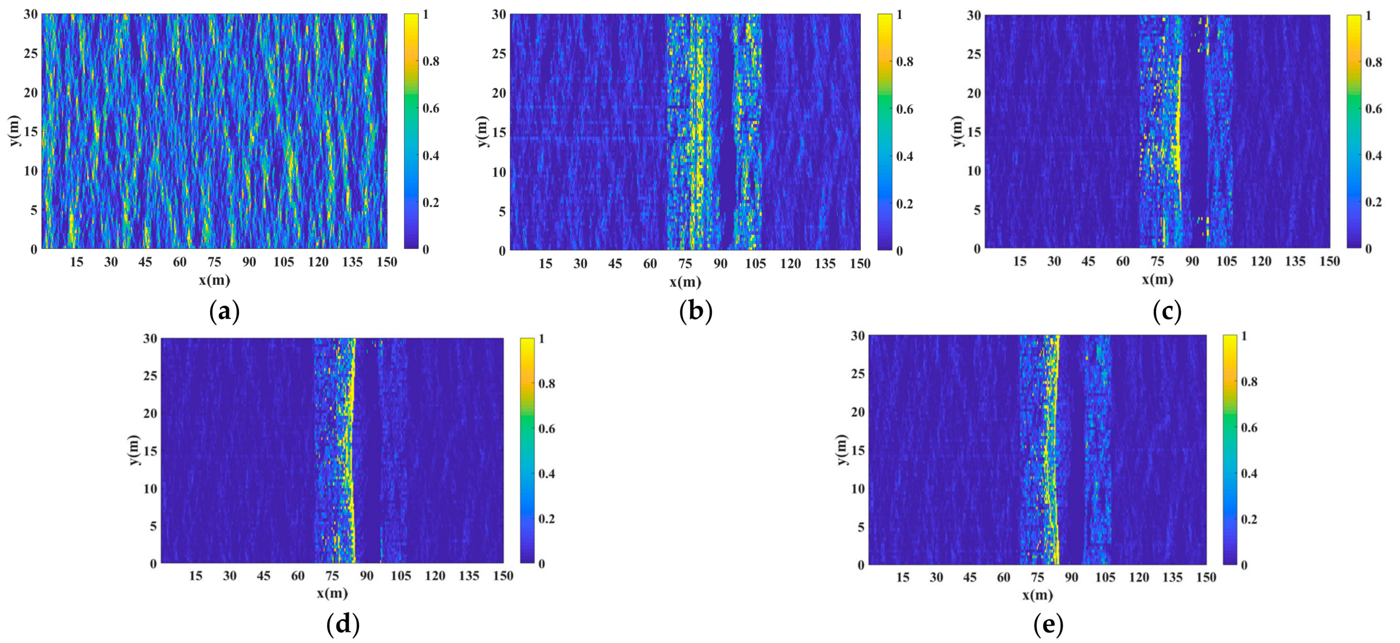


**Figure 17.** Spatial distribution images of the normalized backscattering electric field ($u$ = 10 m/s): (**a**) sea surface, (**b**) sea + plunging breaker: $t = \Delta t$, (**c**) sea + plunging breaker: $t = 6\Delta t$, (**d**) sea + plunging breaker: $t = 10\Delta t$, (**e**) sea + plunging breaker: $t = 14\Delta t$.

### *3.3. HRRP of the 3D Sea Surface with a Plunging Breaker*

Sea-spikes are an abnormal phenomenon of sea clutter with the presence of sharp and short bursts. The characteristics of sea-spike signals are similar to those of targets. Therefore, sea-spikes are usually mistaken as targets and affect target detection and recognition. For this reason, the HRRP of the 3D sea surface with a plunging breaker is further explored. This study is an important attempt because it helps to have some insight into the HRRP characteristics of the 3D sea surface with a plunging breaker and to understand the variation in HRRP during the generation process of a plunging breaker. The contributions are meaningful for target detection and recognition.

Assume that the test model consists of $N$ scattered points and $x_i$ is the location of $i$th scattered point. Scattered far-field of the test model for different frequencies can be expressed as:

$$\vec{E}_s(f) = \sum_{i=1}^{N} A_i \cdot \exp[-j2\pi(\frac{2f}{c})x_i] \tag{13}$$

where $A_i$ is the backscattering intensity of $i$th scattered point.

HRRP can be obtained through the inverse Fourier transform of Equation (13):

$$E_s(x) = F^{-1}\{E_s(f)\} = \int_{-\infty}^{\infty} (\sum_{i=1}^{N} A_i \cdot \exp[-j2\pi(\frac{2f}{c})x_i]) \exp[j2\pi(\frac{2f}{c})x]\mathrm{d}(\frac{2f}{c}) \tag{14}$$

Since the variation range of incident frequency is limited in the real situation, Equation (14) can be represented as:

$$E_s(x) = \sum_{i=1}^{N} A_\mathrm{i} \cdot \int_{f_\mathrm{L}}^{f_\mathrm{H}} \exp[j2\pi(\frac{2f}{c})(x - x_\mathrm{i})]\mathrm{d}(\frac{2f}{c}) \tag{15}$$

where $f_L$ and $f_H$ are the minimum and maximum of incident radar frequency, $j$ represents imaginary number. Let $f_c$ represent the central frequency, and $f_c = (f_L + f_H)/2$. The bandwidth $B = f_H - f_L$.

Then, the HRRP of 3D sea surface with and without a plunging breaker is additionally calculated by the scattered far-field via the CWMFSM and ray tracing hybrid method. The central frequency of incident wave is set as $f_c = 10.0\,\mathrm{GHz}$. The bandwidth is $B = 500\,\mathrm{MHz}$, and the resolution is $\Delta x = 0.3\,\mathrm{m}$. The incident azimuth angle is $\varphi_i = 0°$. HH polarization is considered.

Figures 18 and 19 provide the HRRP with the incident angle $\theta_i = -30°$ and $\theta_i = -80°$, respectively. The wind speed is $u = 7$ m/s. Figures 20 and 21 gives the HRRP simulation results for wind speed $u = 10$ m/s. In Figures 18 and 20, when the incident angle is $\theta_i = -30°$, there is no clear difference between the HRRP of 3D sea surface with and without a plunging breaker. The main reason is that the influence of multipath scattering is weak for a small incident angle, and the intensity of backscattering echo from the plunging breaker region and sea region is close to each other. However, the multipath scattering increases with the incident angle, and the effect of plunging breaker on HRRP. As expected, Figures 19 and 21 demonstrate that the profile of a plunging breaker has a significant influence on the HRRP for a large incident angle. Obviously, the predominant peak is observed, which corresponds to the plunging breaker. For the HRRP of the profiles at $t = \Delta t$ in Figures 19b and 21b, the peak is not as evident as that in Figures 19c–e and 21c–e, because the complicated shape of the plunging breaker is not generated. In contrast, the peaks become sharper at $t = 6\Delta t, 10\Delta t, 14\Delta t$ in Figures 19c–e and 21c–e, where the steep crest is formed. In addition, the location of the peak coincides with the crest of the plunging breaker. It indicates that an increase in the multipath scattering during the generation process of the plunging breaker contributes to the scattering response and HRRP. In general, due to the special geometrical structure of the plunging breaker, sharp peaks appear in the HRRP of the 3D sea surface with a plunging breaker for a large incident angle. The spike behavior is similar to that of a target and may be mistaken as target-like signals. These facts confirm that abnormalities can be observed when a plunging breaker is present on the sea surface. Meanwhile, sea-spikes are noticeable in the HRRP from the sea background, which will increase the false probability of radar. Therefore, the investigation of the HRRP for the 3D sea surface with a plunging breaker will contribute to a further understanding of sea-spikes. Particularly, it is significant for target detection and recognition.

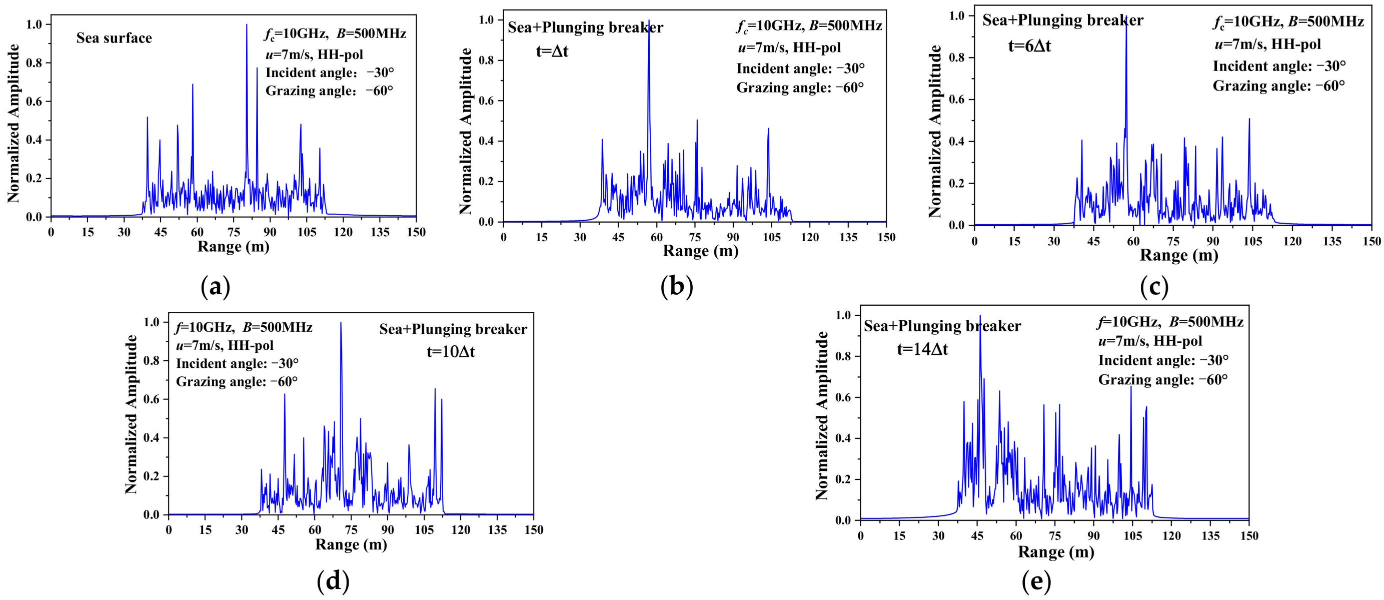


**Figure 18.** HRRP for wind speed $u$ = 7 m/s ($\theta_i = -30°$): (**a**) sea surface, (**b**) sea + plunging breaker: $t = \Delta t$, (**c**) sea + plunging breaker: $t = 6\Delta t$, (**d**) sea + plunging breaker: $t = 10\Delta t$, (**e**) sea + plunging breaker: $t = 14\Delta t$.

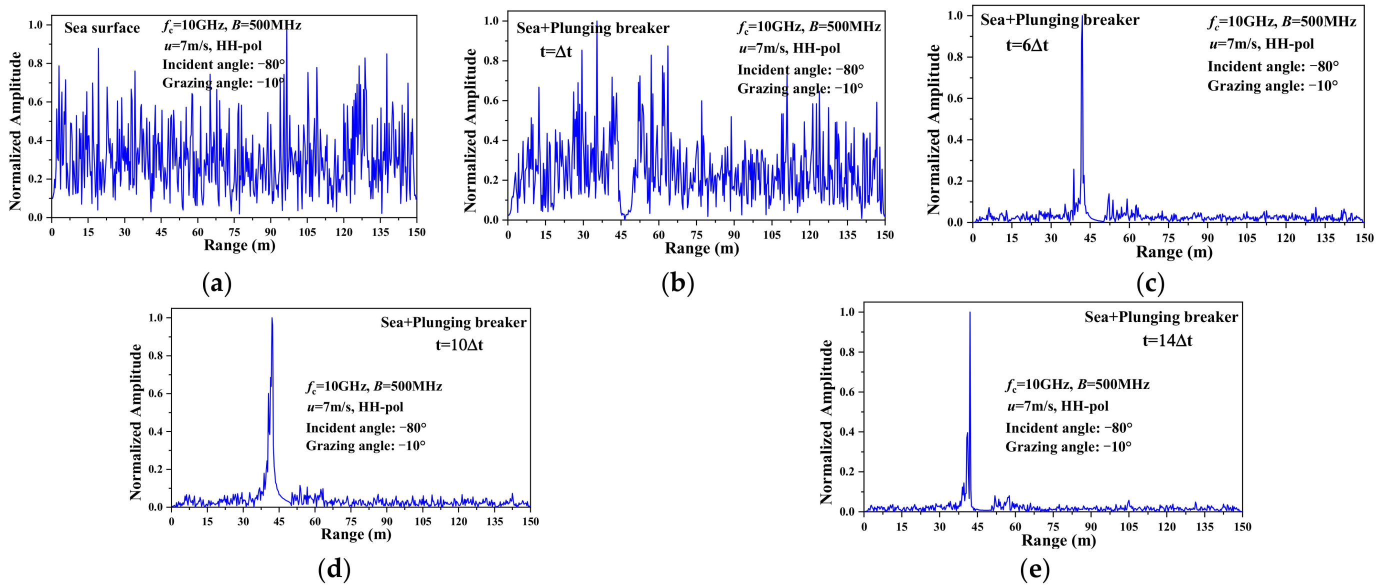


**Figure 19.** HRRP for wind speed $u$ = 7 m/s ($\theta_i = -80°$): (**a**) sea surface, (**b**) sea + plunging breaker: $t = \Delta t$, (**c**) sea + plunging breaker: $t = 6\Delta t$, (**d**) sea + plunging breaker: $t = 10\Delta t$, (**e**) sea + plunging breaker: $t = 14\Delta t$.

Since the plunging breaker backscatter may interfere with the target detection and recognition, it is meaningful to give a comparison of radar scattering characteristics between targets and plunging breakers. In this paper, the HRRP of a simple Perfect Electric Conductor (PEC) target on the sea surface with a plunging breaker is calculated first.

The composite scene and the simulated HRRP are presented in Figure 22a,b, respectively. As shown in Figure 22a, the target consists of two cylinders whose radii are $R_1 = 0.5$ m and $R_2 = 1.0$ m, respectively. The center of the target located at 25.0 m and 15.0 m on $x$ and $y$ axis. The wind speed is $u$ = 10 m/s, and the time sampling point is $t = 14\Delta t$. The other parameters are the same as those of Figure 21. The HRRP in Figure 22b appears as two sharp peaks, which correspond to the target and plunging breaker, respectively. As the scattering intensity of the target is much weaker than that of the plunging breaker, the peak from the plunging breaker is sharper than that of target. In this situation, the plunging breaker will have a strong interference with the target detection and recognition.

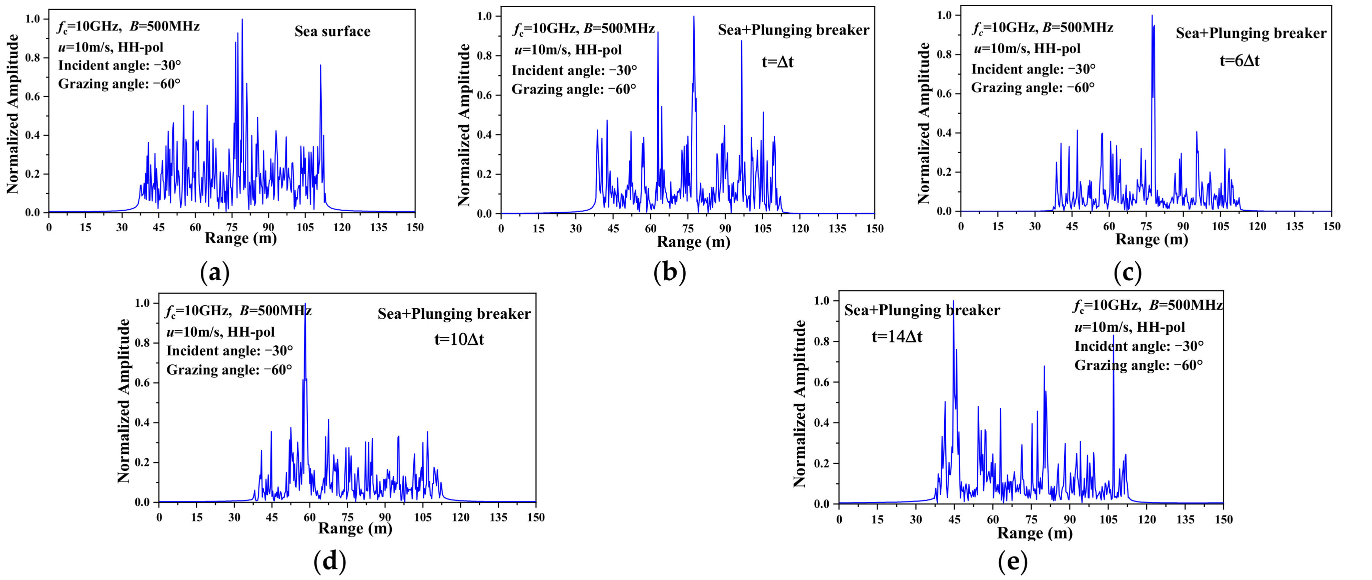


**Figure 20.** HRRP for wind speed $u$ = 10 m/s ($\theta_i = -30°$): (**a**) sea surface, (**b**) sea + plunging breaker: $t = \Delta t$, (**c**) sea + plunging breaker: $t = 6\Delta t$, (**d**) sea + plunging breaker: $t = 10\Delta t$, (**e**) sea + plunging breaker: $t = 14\Delta t$.

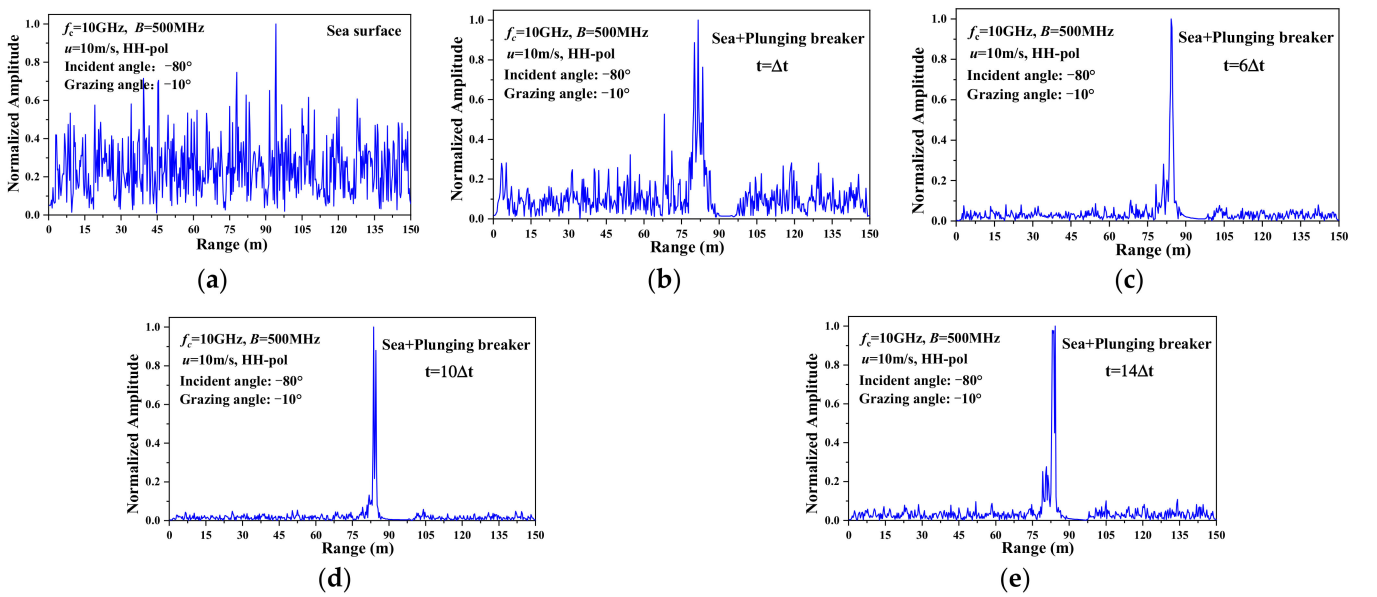


**Figure 21.** HRRP for wind speed $u$ = 10 m/s ($\theta_i = -80°$): (**a**) sea surface, (**b**) sea + plunging breaker: $t = \Delta t$, (**c**) sea + plunging breaker: $t = 6\Delta t$, (**d**) sea + plunging breaker: $t = 10\Delta t$, (**e**) sea + plunging breaker: $t = 14\Delta t$.

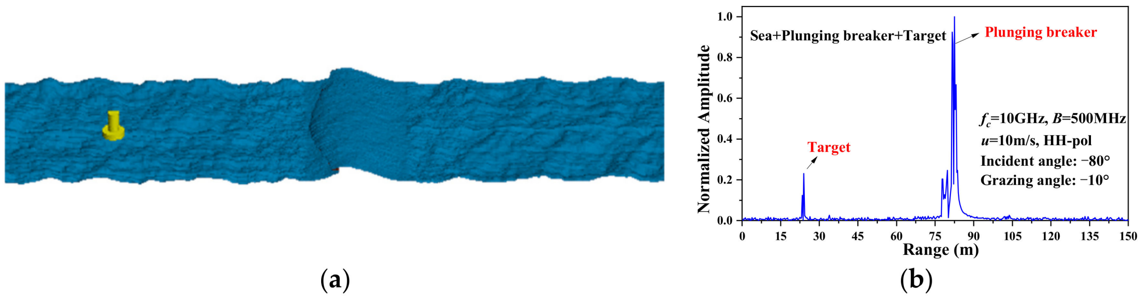


**Figure 22.** The HRRP of a simple target on the sea surface with a plunging breaker: (**a**) The composite scene, (**b**) Simulated HRRP.

Next, the HRRP of a small PEC ship on the sea surface with a plunging breaker for the incident azimuth angle $\varphi_i = 0°$, $10°$, and $30°$ is further studied in Figure 23. The ship is 12.5 m and 2.1 m in length and width. The center of the ship located at 30.0 m and 15.0 m on $x$ and $y$ axis. The other parameters are the same as those of Figure 22. As illustrated in Figure 23b, for the incident azimuth angle $\varphi_i = 0°$, due to the dihedral structure formed by the cabin and deck, the scattering echo from the ship is much stronger than that of the plunging breaker, resulting in that plunging breaker has almost no interference to the HRRP of the ship. However, when the incident azimuth angle changed to $\varphi_i = 10°$ and $\varphi_i = 30°$, as shown in Figure 23c,d, the scattering intensity of the ship is obviously weakened so that the HRRP exhibits sharp peaks in the location of the plunging breaker. Additionally, the plunging breaker will have a strong influence on ship detection and recognition.

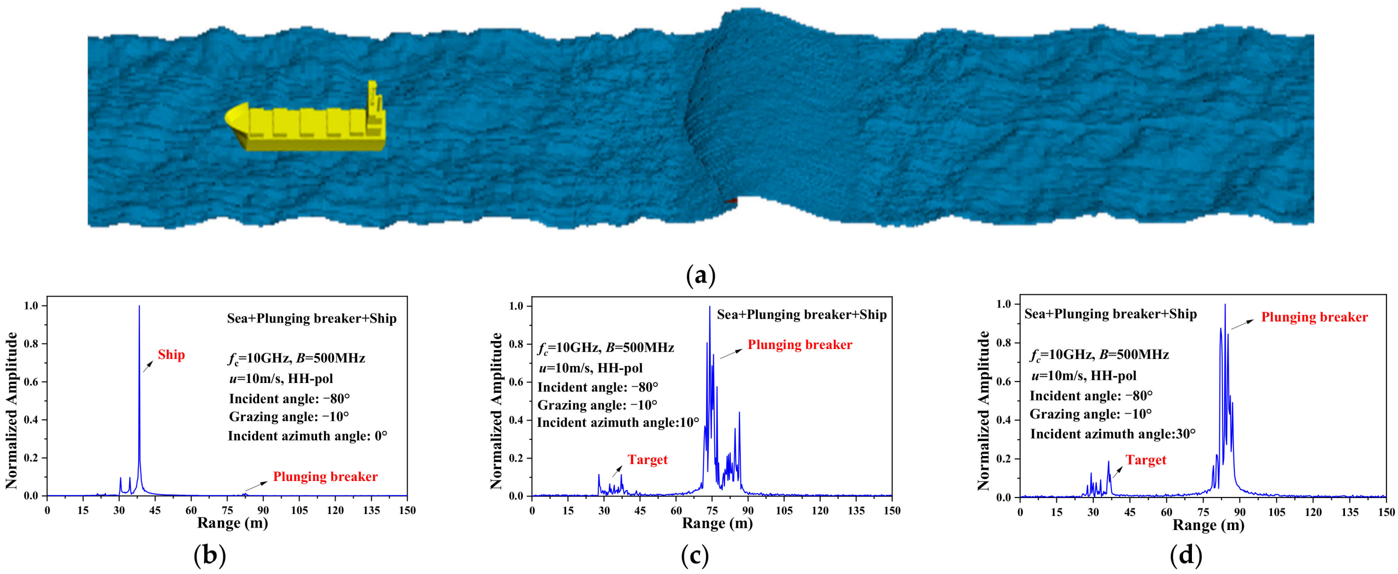


**Figure 23.** The HRRP of a small ship on the sea surface with a plunging breaker: (**a**) The composite scene, (**b**) HRRP for $\varphi_i = 0°$, (**c**) HRRP for $\varphi_i = 10°$, (**d**) HRRP for $\varphi_i = 30°$.

## 4. Conclusions

In this paper, a feasible and wind-related 3D sea surface with a plunging breaker model is constructed. This model can describe the time evolution of a plunging breaker for different wind speeds. On this basis, a hybrid method combing CWMFSM and ray tracing technique is developed to calculate the EM scattering and HRRP of the 3D sea surface with a plunging breaker. According to our simulation results, the following conclusions are obtained:

(1) The plunging breaker is one of the main reasons for the sea-spike phenomenon, which appears to be more obvious during the generation process of a plunging breaker. In addition, the profile of a plunging breaker has a significant effect on the scattering results.

(2) The backscattering RCS varies more dramatically for the upwind incidence than for the downwind incidence when there exists a plunging breaker. Meanwhile, the sea-spike phenomenon is more likely to occur for a large incident angle, upwind incidence, and a high wind speed.
(3) The amplitude of the backscattering electric field from the plunging breaker region is much stronger than that of the sea surface and increases with wind speed. It exhibits sharp and short bursts in the sea background clutter.
(4) For the upwind and large incident angle, noticeable sharp peaks occurred in the HRRP of 3D sea surface with a plunging breaker when the steep crest of the plunging breaker is generated. Moreover, the location of the peak coincides with the crest of the plunging breaker.
(5) A target-like feature is shown in the HRRP of the 3D sea surface with a plunging breaker, which will have a great influence on target detection and recognition.

**Author Contributions:** Methodology, C.D.; Writing—review and editing, X.M.; Validation, J.Z.; Formal analysis, Y.L. and Q.W.; Investigation, L.G. All authors have read and agreed to the published version of the manuscript.

**Funding:** This research was funded by the Fundamental Research Funds for the Central Universities (Grant No. QTZX22161) and the Open Foundation of National Key Laboratory of Electromagnetic Environment (Grant No. 202102008).

**Conflicts of Interest:** The authors declare no conflict of interest.

## References

1. Ulaby, F.T.; Moore, R.K.; Fung, A.K. *Microwave Remote Sensing: Active and Passive: Radar Remote Sensing and Surface Scattering and Emission Theory*; Addison Wesley: Hoboken, NJ, USA, 1982.
2. Bass, F.G.; Fuks, I.M.; Kalmykov, A.I. Very high frequency radiowave scattering by a disturbed sea surface Part I: Scattering from a slightly disturbed boundary. *IEEE Trans. Antennas Propag.* **1968**, *16*, 554–559. [CrossRef]
3. Bass, F.G.; Fuks, I.M.; Kalmykov, A.I. Very high frequency radiowave scattering by a disturbed sea surface Part II: Scattering from an actual sea surface. *IEEE Trans. Antennas Propag.* **1968**, *16*, 560–568. [CrossRef]
4. Qiao, T.; Tsang, L.; Vandemark, D. Sea Surface Radar Scattering at L-Band Based on Numerical Solution of Maxwell's Equations in 3-D (NMM3D). *IEEE Trans. Geosci. Remote Sens.* **2018**, *56*, 3137–3147. [CrossRef]
5. Melief, H.W.; Greidanus, H.; Genderen, P.V. Analysis of sea spikes in radar sea clutter data. *IEEE Geosci. Remote Sen. Lett.* **2006**, *44*, 985–993. [CrossRef]
6. Posner, F.; Gerlach, K. Sea spike demographics at high range resolutions and very low grazing angles. In Proceedings of the 2003 IEEE Radar Conference, Huntsville, AL, USA, 8 May 2003.
7. Smith, M.J.; Poulter, E.M.; McGregor, J.A. Doppler radar measurements of wave groups and breaking waves. *J. Geophys Res.* **1996**, *101*, 14269–14282. [CrossRef]
8. Rosenberg, L. Sea-spike detection in high grazing angle X-band sea-clutter. *IEEE Trans. Geosci. Remote Sens.* **2013**, *51*, 4556–4562. [CrossRef]
9. Rino, C.L.; Ngo, H.D. Numerical simulation of low-grazing-angle ocean microwave backscatter and its relation to sea spikes. *IEEE Trans. Antennas Propag.* **1998**, *46*, 133–141. [CrossRef]
10. Sletten, M.A.; West, J.C.; Liu, X.; Duncan, J.H. Radar investigations of breaking water at low grazing angles with simultaneous high-speed optical imagery. *Radio Sci.* **2003**, *38*, 18-1–18-17. [CrossRef]
11. Wang, P.; Yao, Y.; Tulin, M.P. An efficient numerical tank for nonlinear water waves, based on the multi-subdomain approach with BEM. *Int. J. Numer. Methods Fluids* **1995**, *20*, 1315–1336. [CrossRef]
12. Holliday, D.; Deraad, L. Sea-spike backscatter from a steepening wave. *IEEE Trans. Antennas Propag.* **1998**, *46*, 108–113. [CrossRef]
13. West, J.C. Low-grazing-angle (LGA) sea-spike backscattering from plunging breaker crests. *IEEE Trans. Geosci. Remote Sens.* **2002**, *40*, 523–526. [CrossRef]
14. West, J.C.; Ja, S.J.; Duncan, J.H.; Qiao, H. LGA scattering from breaking water waves-further results. In Proceedings of the IEEE 1999 International Geoscience and Remote Sensing Symposium, Hamburg, Germany, 28 June–2 July 1999.
15. West, J.C. Ray analysis of low-grazing scattering from a breaking water wave. *IEEE Trans. Geosci. Remote Sens.* **1999**, *37*, 2725–2727. [CrossRef]
16. Zhao, Z.Q.; West, J.C. Extended GO modeling of microwave backscattering from measured breaking wave crests. In Proceedings of the 2003 IEEE International Geoscience and Remote Sensing Symposium, Toulouse, France, 21–25 July 2003.
17. West, J.C.; Zhao, Z.Q. Electromagnetic modeling of multipath scattering from breaking water waves with rough faces. *IEEE Trans. Geosci. Remote Sens.* **2002**, *40*, 583–592. [CrossRef]

18. West, J.C.; Sturm, M.J.; Ja, S.J. Low-grazing scattering from breaking water waves using an impedance boundary MM/GTD approach. *IEEE Trans. Antennas Propag.* **1998**, *46*, 93–100. [CrossRef]
19. Yang, W.; Zhao, Z.; Qi, C.; Nie, Z. Electromagnetic modeling of breaking waves at low grazing angles with adaptive higher order hierarchical legendre basis functions. *IEEE Trans. Geosci. Remote Sens.* **2011**, *49*, 346–352. [CrossRef]
20. Li, Y.Z.; West, J.C. Microwave scattering from 3-D breaking water wave crests. In Proceedings of the 2004 IEEE International Geoscience and Remote Sensing Symposium, Anchorage, AK, USA, 20–24 September 2004.
21. Li, Y.Z.; West, J.C. Low-grazing-angle scattering from 3-D breaking water wave crests. *IEEE Trans. Geosci. Remote Sens.* **2006**, *44*, 2093–2101.
22. Zhao, Z.Q.; West, J.C. Low grazing angle microwave scattering from a three-dimensional spilling breaker crest: A numerical investigation. *IEEE Trans. Geosci. Remote Sens.* **2005**, *43*, 286–294. [CrossRef]
23. Zhao, Z.Q.; West, J.C. Two-scale analysis of LGA scattering from a 3-D spilling breaker crest. In Proceedings of the IEEE Antennas and Propagation Society International Symposium, Columbus, OH, USA, 22–27 June 2003.
24. Jeschke, S.; Birkholz, H.; Schumann, H. *A Procedural Model for Interactive Animation of Breaking Ocean Waves*; UNION Agency Science Press: Plzen, Czech Republic, 2003; Volume 14, pp. 17–20.
25. Zhang, M.; Chen, H.; Yin, H.C. Facet-based investigation on EM scattering from electrically large sea surface with two-scale profiles: Theoretical model. *IEEE Trans. Geosci. Remote Sens.* **2011**, *49*, 1967–1975. [CrossRef]
26. Li, W.L.; Guo, L.X.; Meng, X.; Liu, W. Modeling and electromagnetic scattering from the overturning wave crest. *Acta Phys. Sin.* **2014**, *63*, 164102.
27. Elfouhaily, T.; Chapron, B.; Katsaros, K.; Vandemark, D. A unified directional spectrum for long and short wind-driven waves. *J. Geoph Res.* **1997**, *102*, 15781–15796. [CrossRef]
28. Voronovich, A.G.; Zavorotny, V.U. Theoretical model for scattering radar signals in Ku- and C-bands from a rough sea surface with breaking wave. *Waves Random Media* **2001**, *11*, 247–269. [CrossRef]
29. Meissner, T.; Wentz, F.J. The complex dielectric constant of pure and sea water from microwave satellite observations. *IEEE Trans. Geosci. Remote Sens.* **2004**, *42*, 1836–1849. [CrossRef]
30. Ling, H.; Chou, R.C.; Lee, S.W. Shooting and bouncing rays: Calculating the RCS of an arbitrarily shaped cavity. *IEEE Trans. Antennas Propag.* **1989**, *37*, 194–205. [CrossRef]
31. Dehmollaian, M.; Sarabandi, K. Electromagnetic scattering from foliage camouflaged complex targets. *IEEE Trans. Geosci. Remote Sens.* **2006**, *44*, 2698–2709. [CrossRef]
32. Jin, K.S.; Suh, T.I.; Suk, S.H.; Kim, B.-C.; Kim, H.-T. Fast ray tracing using a space-division algorithm for RCS prediction. *J. Electromagn. Waves Appl.* **2006**, *20*, 119–126. [CrossRef]
33. Dong, C.L.; Guo, L.X.; Meng, X.; Wang, Y. An accelerated SBR for EM scattering from the electrically large complex objects. *IEEE Antennas Wireless Propag. Lett.* **2018**, *17*, 2294–2298. [CrossRef]